

Nanodefekt-controlled permeation in AlO_x/polymer gas barrier films

Vincent R. Tobin, Hélène Suttle & Hazel E. Assender

Department of Materials, University of Oxford, 16 Parks Road, Oxford, OX1 3PH

Corresponding author: hazel.assender@materials.ox.ac.uk

Abstract

The permeation of water vapour through a coated polymer gas barrier film is controlled by the defects in the coating. By modelling these defects as a combination of macro-defects (in which the activation energy of permeation is that of the underlying polymer substrate) and nano-defects (in which the activation energy of permeation is something greater than that of the polymer substrate), we are able to understand the mechanisms of permeation in high gas barrier layers. Permeation is controlled by the amounts of such defects, with the observed overall activation energy informing us of the relative permeation through macro- and nano- defects. Three examples of Aluminium oxide (AlO_x)-coated polymers are given to illustrate this: a comparison of poly(ethylene naphthalate) and polypropylene (OPP) substrates, the role of sputter power in AlO_x/OPP films and the role of oxide thickness in AlO_x/OPP films. When the amount of permeation through macro-defects is quite low, and hence nano-defect permeation is a significant proportion of the overall water vapour transport, control of each of the two defect types becomes important. Contrary to what has been previously assumed, the activation energy can be observed as greater in some cases in which the overall permeation is also greater, and this can be explained by an increase in the proportion of permeation taking place through nanodefects. This model is evidenced by reference to microstructural and other characterisation, and hence gives rise

to understanding of the relationship between process properties, microstructure and permeation.

Keywords

Gas barrier, defects, polymer, WVTR, activation energy

1. Introduction

Ceramic layers on polymer substrates are used as transparent gas barrier films for packaging and encapsulation of sensitive products, and are of particular interest for the manufacture of flexible thin film optoelectronics components, for which control of the transport of water vapour is particularly pertinent [1]. Various different deposition methods and materials can be applied, as reviewed by Park et al [2] and with recent particular interest in PE-CVD [3,4] and ALD [5-9] deposition and also novel materials e.g. [10], and it is important to understand and control the permeation pathways that arise from the resulting materials. The ceramic layer acts to cover over the flexible polymer substrate, which is typically much more permeable, but defects in this thin ceramic layer allow substantially more permeation through the composite than would be expected from a perfect thin layer. Measurements of permeation as a function of temperature introduced use of the activation energy, ΔE , of permeation to characterise the permeation pathways [11-13]. Roberts *et al.* [14] categorised possible permeation pathways by size and nature, and here we define 'macro-defects', which are sufficiently large for permeant molecules to pass through them unhindered, or 'nano-defects', where there is some interaction of the permeant with the defect wall or amorphous matrix of the ceramic. Microstructural characterization of typical layers reveals evidence of macrodefects in the form of holes, scratches etc., as well as an overall microstructure of agglomerates [15-20]. Where permeation is dominated by macro-

defects, the ΔE for permeation through the composite is that of the polymer, as the permeant flux is only controlled by its passage through the underlying polymer substrate. The gas transmission rate, GTR , will be substantially lower than uncoated polymer, however, as the ceramic layer serves to cover over most of the surface area with far less permeable material, and the permeation observed is only due to the much smaller, uncoated, areas contained within the defects, drawing gas from the substrate area close to the defect. Gas permeating through the substrate from areas far from such a defect will have to travel a significant distance through the substrate to reach the defect giving rise, in effect, to a negligible concentration gradient along this longer path to give rise to flux. In films where permeation through macro-defects is no longer the dominant process, a significant proportion of the permeation is through nano-defects or the amorphous matrix of the coating, so the ΔE measured for the composite increases to a value above that of the polymer. An observed increase in activation energy is often associated with an observed decrease in GTR : as the macro-defect density is reduced, there is less permeation overall, and a greater proportion of the gas which does permeate does so through nano-defects, as the macro-defects can no longer be reached.

In this paper, to illustrate cases in which nano-defect permeation becomes significant, we consider the water vapour permeation through high barrier films consisting of Aluminium Oxide (AlOx) sputtered onto substrates of orientated polypropylene (OPP) and poly(ethylene naphthalate) (PEN). Our films have a sufficiently low density of macro-defects that these no longer completely dominate the permeation. We show how the ΔE and water vapour transmission rate, $WVTR$, can be changed by changes in substrate nature and process conditions, which in turn alter the ratio of the permeation through macro- and

nano- defects. We give examples in which the overall permeation of the barrier *increases*, despite an increase in activation energy.

GTR (in our case, the *WVTR*) is defined as the amount of permeant passing through the barrier film per unit area per unit time and this can be normalised for layer thickness by considering the permeability, P :

$$P = \frac{GTR.t}{\Delta p} \quad (1)$$

where t is the thickness of the film and Δp is the pressure difference across the film. The barrier improvement factor, *BIF*, [21] of a composite film is the ratio of the *GTR* of the substrate to the *GTR* of the composite. The permeability of defect-free separate layers of the composite can be calculated using ideal laminate theory [22]:

$$P_{ILT} = \left(\frac{\varphi_p}{P_p} + \frac{\varphi_g}{P_g} \right)^{-1} \quad (2)$$

where φ_p and P_p , and φ_g and P_g , are the volume fractions and permeabilities of the polymer and ceramic glass respectively.

Roberts [14] modelled the permeability of a composite barrier, P_b , in which there were defects, as the sum of the permeability due to macro-defects and the permeability of the Ideal-Laminate material between these defects:

$$P_b = C_{md}P_p + \left(\frac{\varphi_p}{P_p} + \frac{\varphi_g}{P_{la}+P_{nd}} \right)^{-1} \quad (3)$$

where C_{md} is a dimensionless constant that depends on the size and number of macro-defects in the film, and P_{la} and P_{nd} are the permeabilities of the amorphous matrix and nano-defects respectively.

This approach assumes a uniform concentration of water in the sample across its whole area i.e. it does not take into account, for example, that macro-defects may locally deplete the water in the film and hence modify the flux of permeant through neighbouring defects. Recent numerical models have sought to describe the effect local permeant concentration which is important when considering the effect of the shape and distribution of defects [23-25].

Transport of permeant is temperature dependent and is described by the Arrhenius equation [11-13]:

$$P = P_0 e^{-\frac{\Delta E}{RT}} \quad (4)$$

where R is the gas constant, T is the absolute temperature and P_0 is a pre-exponential factor (i.e. the notional permeability at infinite temperature).

Roberts *et al.* [14] modelled the relative contributions of P_{la} and P_{nd} by consideration of the permeation of a range of inert gases of various size. In our case, in which only water vapour is considered, we will group the matrix permeation with nano-defect permeation to consider only that permeation that will show an activation energy equal to that of the polymer ('macro-defect') and all other permeation, in which the water molecules will interact with the ceramic during permeation, and hence have a greater activation energy ('nano-defect'). Thus, the temperature-dependant *WVTR* of the composite will be the sum of the *WVTR* through the macro-defects (with activation energy that of the polymer

substrate, ΔE_p) and the $WVTR$ through the nano-defects (with activation energy ΔE_n). Thus, as Henry *et al.* pointed out [26], the apparent activation energy of the composite, ΔE_c , will lie between the extremes, ΔE_p and ΔE_{nd} . This can be described by:

$$WVTR_c = WVF_{md} e^{-\left(\frac{\Delta E_p}{RT}\right)} + WVF_{nd} e^{-\left(\frac{\Delta E_{nd}}{RT}\right)} \quad (5)$$

where $WVTR_c$ is the permeation of the composite, WVF_{md} and WVF_{nd} are the pre-exponential factors for permeation through macro-defects and nano-defects respectively, which will be proportional to the number and size of such defects. This analysis, therefore, describes the total permeation due to each type of defect in terms of the total area of polymer substrate overlaid with this type of defect, but does not describe the number, distribution or nature of these defects. In particular, the nano-defects present may well have a range of sizes, tortuosity and surface chemistries, and therefore a range of activation energies and transport rates, but this analysis groups all such defects together under single effective values for ΔE_{nd} and WVF_{nd} .

This composite $WVTR_c$ does not fit the function:

$$WVTR_c = K e^{-\left(\frac{\Delta E_c}{RT}\right)} \quad (6)$$

over all temperatures, however in the narrow range of temperatures that can be measured experimentally, a plot of $\ln(WVTR_c)$ against $1/T$ does show a linear relationship within experimental error, so an apparent value of ΔE_c can be determined, as illustrated in Figure 1. The trace for the uncoated polymer is shown in Figure 1 with black diamonds. The gradient depends on ΔE_p , and the intercept on the vertical axis on $WVTR_o$. If there were a population of macro-defects, but no nano-defects (grey circles) the gradient is that of the uncoated polymer, but the intercept is lower, reflecting the smaller area of polymer, within

the macro-defects, through which there is easy permeation. If there were no macro-defects and a large population of nano-defects (grey triangles) the gradient is steeper, reflecting the greater energy barrier to permeation through the nano-defects. The total permeation trace (black squares) is the sum of these two, weighted for the relative population. The apparent ΔE_c can be determined from the gradient within the experimental window (blue dashed line).

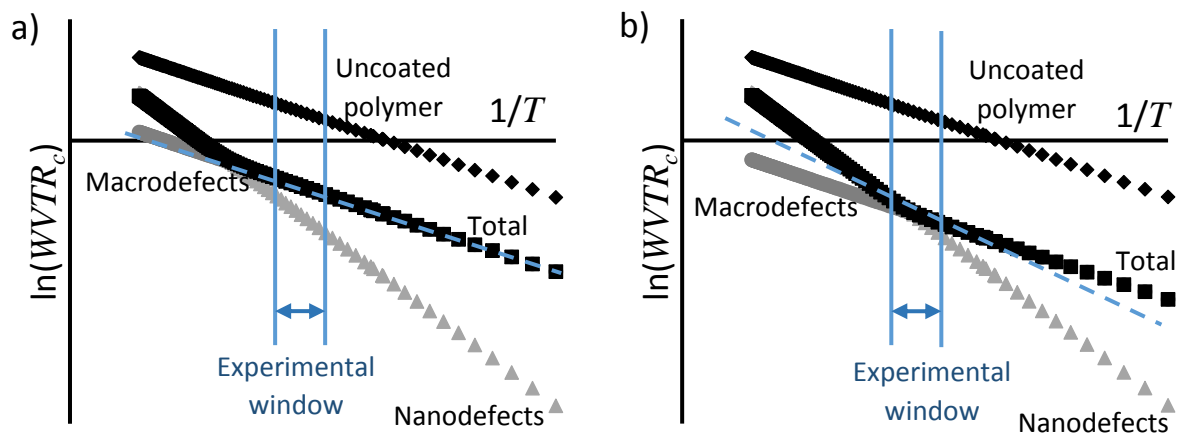


Figure 1 Schematic of $\ln(WVTR_c)$ vs $1/T$ plots to illustrate the overall composite performance. All points are generated from equation 5 with appropriate parameters. Black diamonds – substrate permeation, black squares – composite permeation, grey circles – macrodefect permeation, grey triangles – nanodeflect permeation. (a) Example with a large amount of macro-defects. (b) Example with a small amount of macro-defects and a larger amount of nano-defects.

Figure 1(a) illustrates the case where the population of macro-defects is high (as is often the case elsewhere in the reported literature), so the crossover-point between the pure macro-defect and pure nano-defect cases in Figure 1 will be to the left (higher temperatures) of the

experimentally accessible range of temperatures. Thus, the apparent activation energy observed at standard temperatures is that of the polymer, and the $WVTR_c$ is determined by the amount of macro-defects. When the population of macro-defects is such that not all permeation is dominated by transport through macro-defects, the kink in the total permeation curve will move to the right (towards lower temperatures), and ultimately to the case (Figure 1(b)) where in the experimental window of temperatures, both the macro-defects and nano-defects are influencing the activation energy and permeation. As the proportion of permeation occurring through the nano-defects increases, the gradient observed in the experimental window will increase, eventually to approach that of pure nano-defect permeation.

2. Experimental details

Two polymer substrates were used for barrier layers: PEN of thickness 125 μ m tailored to have a very smooth upper surface (Teonex Q65, DuPont Teijin) to receive a barrier coating, and bi-axially oriented polypropylene of thickness 90 μ m (Rayoart CG 90, Innovia Films) that does not have such surface conditioning.

Aluminium oxide (AlO_x) barrier coatings were deposited by RF magnetron reactive sputtering from Al targets (Angstrom Sciences) in a roll-to-roll vacuum webcoating facility (Aerre Machines). Substrates were taped to a drum (cylinder width 350mm, circumference 2m) rotating at 25 rpm, meaning that during a single deposition run, the sample passes the sputter cathodes multiple times, building up a single, thick, oxide layer made up of multiple sublayers. The deposited layers have an optical transmission between 85% and 90% (90% being typical transmission of the uncoated substrate). Previous work [17,15,27] has reported a drop in barrier performance associated with thicker monolithic layers, which was

thought to be due to the build-up of residual stresses [28], leading to the formation of defects in the barrier layer. In our case, the multiple pass process reduces the build-up of internal stresses (for example, there is little or no ‘curling’ of the films on demounting them post-deposition), and hence allows very thick layers to be deposited with increasingly high barrier properties (Figure 2).

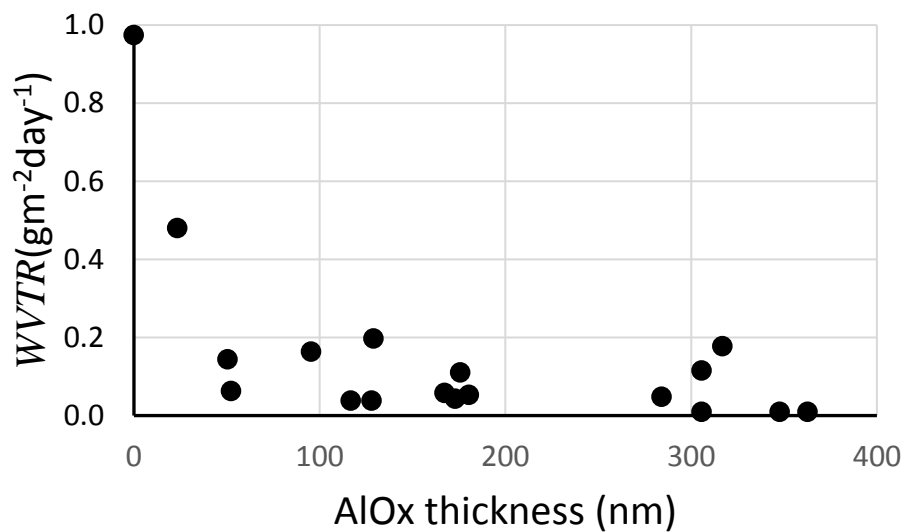


Figure 2 WVTR over a wide range of coating thickness of AlOx on PEN indicating no loss in barrier even for very thick coatings, where the coating was deposited by sputtering by multiple passes of the sputtering source.

In order to produce highly transparent layers, oxygen was introduced into the sputter argon plasma at the maximum flow rate possible before the targets ‘poisoned’ by oxidation (on poisoning the voltage of the power-controlled supply dropped and the deposition rate decreased substantially). Sputtering after the poisoning point has been associated with lower barrier performance due to microarcing of the insulating cathodes, introducing defects in the barrier [29]. This poisoning point was established before each set of samples, and was typically around 15 sccm of oxygen with an argon flow rate of 200 sccm. These

sputtered layers are known to be amorphous [30] and ToF SIMS measurements of these coatings with multiple sub-layers showed that they were uniform through the thickness, with no compositional variation associated with the sublayers (Figure 3).

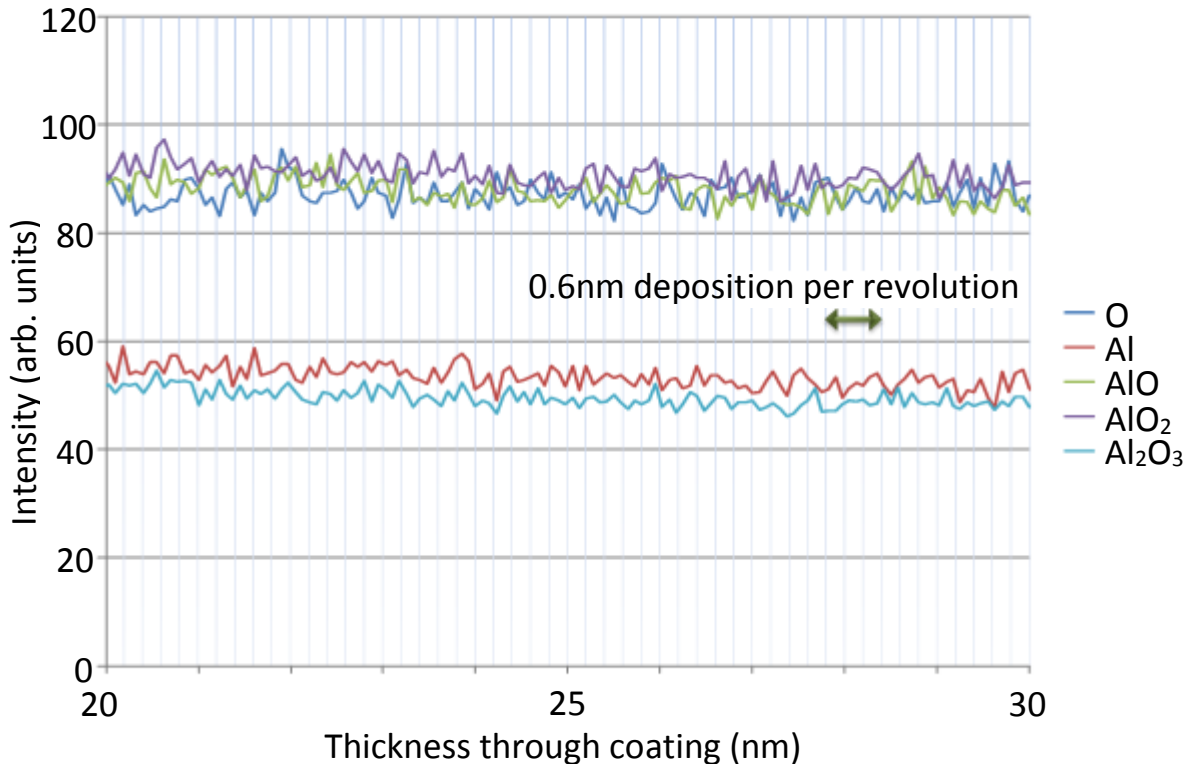


Figure 3 ToF SIMS high resolution depth profile showing a section through the AlO_x coating.

The arrow indicates the thickness of material deposited during one rotation of the drum.

ToF SIMS measurements were carried out through the University of Nottingham Open Access Project on a ToF-SIMS IV from ION-TOF GMBH, Münster, Germany, equipped with a liquid metal ion gun (Ga^+) for spectroscopy and a Cs^+ for depth profiling (5kV for 5s with 1s pause for analysis). The area milled by Cs^+ ($250\ \mu m \times 250\ \mu m$) was significantly larger than that analysed ($100\ \mu m \times 100\ \mu m$) to avoid edge effects.

Surface topography of substrates and coatings was imaged using Ominscan MicroXAM 5000B 3d ADE Phase shift interference contrast optical profiler, and Veeco Autoprobe and Agilent 5400 atomic force microscopes (with MicroMasch NSC35 cantilevers). Coating thickness was measured using a Rudolph Auto EL ellipsometer on films deposited onto fragments of silicon wafer placed alongside the polymer during deposition.

WVTR was recorded using the MOCON Permatran W 3/31 (ASTM F-1249) at 35°C, 38°C, 44°C and 50°C at 100%RH with a sample size 50cm³. Ca test measurements were carried out to qualitatively assess the permeation. Four 2cm diameter discs of Ca were evaporated onto the coated side of the barrier films in an Edwards 306 evaporator (2-5 x 10⁻⁵ mBar at deposition rate of 0.3-0.6 nm s⁻¹) located within a nitrogen atmosphere glovebox. 3mm thick float glass squares (cleaned with isopropanol, water and then dried in a vacuum oven for at least three hours) were adhered to the barrier layer with the Ca layer on the glass side using about 20ml of epoxy (Electro-lite Corporation, ELC-2500) cured with a hand-held UV lamp (Intertronics IUUV250). In this way, any water vapour that degrades the reflective Ca to transparent Ca(OH)₂ must permeate through the barrier composite. The Ca spots were photographed (Olympus SP-320 camera) at appropriate intervals with the sample lit in transmission. Between photographs, the samples were stored in an oven held at 38°C with 85%RH atmosphere (equilibrated with a saturated aqueous solution of potassium chloride). Samples sealed between two layers of glass were shown to have no deterioration of the Ca beyond the lifetime of the experiments.

3. Results and discussion

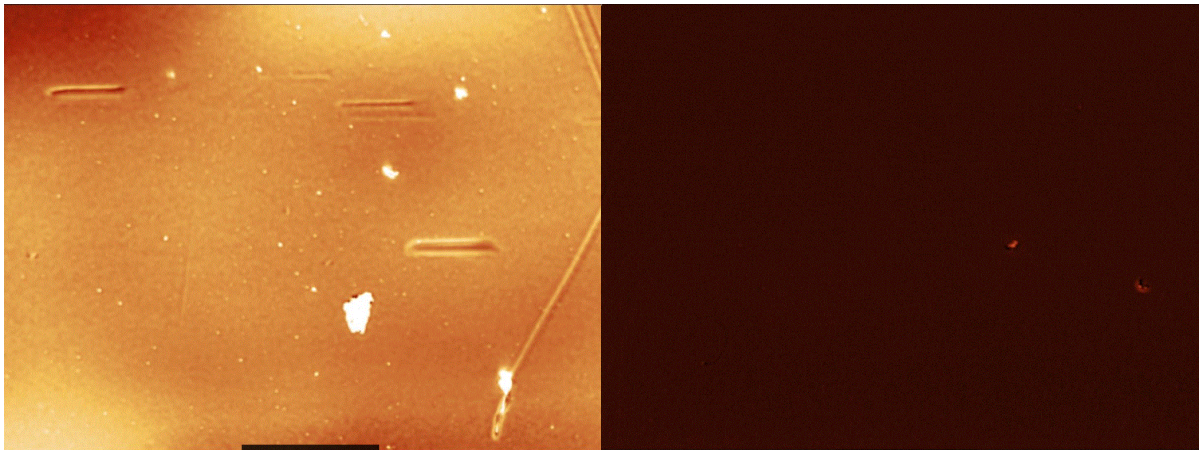
3.1 Comparison of OPP and PEN substrates

AlOx layers on two, contrasting, polymer substrates are compared. One is a PEN developed for flexible electronics application with a highly smooth surface onto which the AlOx is deposited, the other a biaxially oriented OPP for graphic art or label applications, with a much rougher surface onto which the AlOx is deposited, which might be expected to give rise to a greater defect density in the sputtered ceramic layers.

Optical profilometry images of the oxide deposited on the different substrates (Figure 4) illustrates the contrasting morphologies. The images of Figure 4 show a population of protrusions 200nm-2 μ m high (i.e. comparable to thickness of the oxide layer) on the surface, reflecting those observed on the substrate. These may be the origin of macro-defects in the barrier layer [17]. The Teonex substrate is largely featureless because of its deliberately high quality surface finish. Even between these large defects, the surface of the Teonex is much smoother than that of the OPP, which is reflected in a significantly smoother oxide between the large protrusions (compare Figure 4(c) and (d)).

a) OPP/AlOx

b) PEN/AlOx



c) OPP/AlOx

d) PEN/AlOx

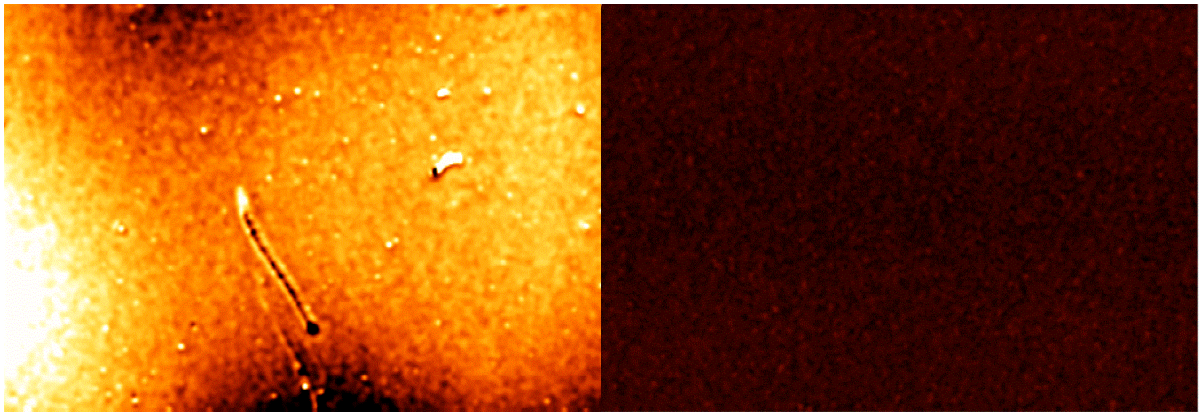


Figure 4 Optical profilometry images of a) an OPP/AlOx surface (example of a 'general view'), b) a PEN/AlOx (example of a 'general view') showing only two asperities in this field of view, c) an OPP/AlOx surface taken from an area of the surface without asperities over $1\mu\text{m}$ in height, d) a PEN/AlOx surface taken from an area without the larger surface asperities. For direct comparison, the images in (a) and (b) are plotted from an area $170\mu\text{m} \times 130\mu\text{m}$ with a z-scale of $1\mu\text{m}$: asperities over $1\mu\text{m}$ in height are shown white, and those in (c) and (d) from an area of $100\mu\text{m} \times 60\mu\text{m}$ with a z-scale of $0.2\mu\text{m}$.

Surface roughnesses of the substrate and the subsequent oxides, deposited at 1.85 kW sputtering power, are summarized in Table 1.

Table 1 Summary of RMS roughness of polymer substrates and the oxide layers deposited on them. Each roughness from a 'general view' was measured from optical profilometry images of area 170 μ m x 130 μ m. In addition, the roughness is measured from a smaller area, selected to be in an area away from the largest asperities ('smooth' area) to indicate the underlying roughness of the substrate. A 10th order polynomial background substitution has been applied to remove the long wavelength waviness in the surface which will not contribute to defects in the oxide that are associated with increased permeation.

Sample	RMS Roughness (nm), general view	RMS Roughness (nm) of 'smooth' area
OPP	48, 22	24
OPP/AIO_x	73, 25	17
PEN	3.5	3.5
PEN/AIO_x	2.9, 5.8	2.9

The substrates give rise to different barrier properties (Table 2). The underlying water vapour permeability of the PEN is greater than OPP due to its greater hydrophilicity. Oxide deposited on the PEN performs better as a barrier than that deposited on the OPP: the *BIF* and the calculated permeability of the coating is superior in the case of PEN.

Table 2 Summary of water vapour permeation properties, comparing the different substrates. The permeability of the coating is calculated from the measured permeation of the composite using ideal laminate theory. The lowest value of permeation is taken for the permeability calculation and subsequent analysis, as this is least likely to have been affected by any defects that may be induced by sample handling.

Film	Thickness (μm)	WVTR at 38°C ($\text{g}/\text{m}^2/\text{day}$)	ΔE_c (kJ/mol)	BIF	Permeability ($\mu\text{m. g}/\text{m}^2/\text{day}$)
OPP	90	1.43	67	-	129
OPP / AlO_x	90 + 0.145	0.38	104	4	0.075 (coating)
PEN	125	1.46	54	-	183
PEN / AlO_x	125 + 0.148	0.054,0.076	84,95	19-27	0.0083 (coating)

The activation energies of the films with a barrier coating are significantly greater than that of the underlying substrate in both cases – permeation is not dominated by transport through macro-defects in either case. Surprisingly, the permeability of the coating on PEN is nearly an order of magnitude lower (better) than that on OPP, despite the OPP exhibiting a greater activation energy, in contrast to Erlat’s examples [16]. This can be explained if the OPP sample is considered to have a greater proportion of the water vapour passing through nano-defects than the PEN, giving rise to the increased activation energy, while at the same time having an overall greater amount of defects, giving rise to the greater WVTR. There are three unknown variables in equation 5, WVF_{md} , WVF_{nd} and ΔE_{nd} , and two equations that can be derived from the experimental data: equation 5 (e.g. at 38°C, as quoted in table 2), and the gradient of the $\ln WVTR_c$ vs $1/T$ plot, which gives rise to the apparent activation energy. Table 3 gives example solutions based on the assumption that for both substrates $\Delta E_{nd} = 130 \text{ kJmol}^{-1}$. The *proportion* of water vapour transmitted through nano-defects is

greater in the OPP case, giving rise to the greater composite activation energy, but the *amount* permeation due to the defects, for each of macro- and nano-, is greater for the OPP, and hence the overall *WVTR* is also greater. Hence this example illustrates how, in cases where there is a balance of permeation between both macro- and nano-defects, the activation energy can be greater even in cases of a more permeable composite.

Table 3 Example data for a model of WVTR and ΔE_c , comparing the data for AlOx barriers, sputtered at 1.85 kW, on OPP and PEN from Table 2. The values of ΔE_p are determined from permeation measurements on the uncoated polymer. The value of ΔE_{nd} is arbitrarily set, and, in this case, kept identical for the two polymer substrates.

		OPP/AlOx	PEN/AlOx
Macrodefects	WVF_{md} (g/m ² /day)	3.6×10^{10}	4.3×10^7
	ΔE_p (kJ/mol) [†]	67	54
	$WVTR_{md}$ at 38°C (g/m ² /day)	0.20	0.04
Nanodefects	WVF_{nd} (g/m ² /day)	12.4×10^{20}	0.9×10^{20}
	ΔE_{nd} (kJ/mol)	130	130
	$WVTR_{nd}$ at 38°C (g/m ² /day)	0.18	0.01
Total	$WVTR_c$ at 38°C (g/m ² /day)	0.38	0.05
	ΔE_c (kJ/mol)	104	84
	$WVTR_{nd}/WVTR_c$	48%	27%

[†] Calculated from uncoated polymer substrate data in Table 2

Ca test images of this material agree (Figure 5) with the *WVTR* measurements: the more rapid decay of the Ca (i.e. the brightening of the images) is consistent with the greater $WVTR_c$ of the OPP/AlOx film. The morphology observed differs, however, in a manner consistent with the hypothesis of defect populations. The PEN/AlOx shows discrete brighter areas associated with a certain density of defects (likely, the macro-defects in this case). The background greying of the film (likely due to permeation through nano-defects) is much

slower than that of the OPP sample as there is lower overall permeation, spread over a larger area, through the nano-defects between these macro-defects. The more general greying of the OPP sample can be associated with the far greater density of defects, both macro- and nano-, in the AlOx on OPP, meaning that permeation locations cannot be individually resolved by the optical imaging.

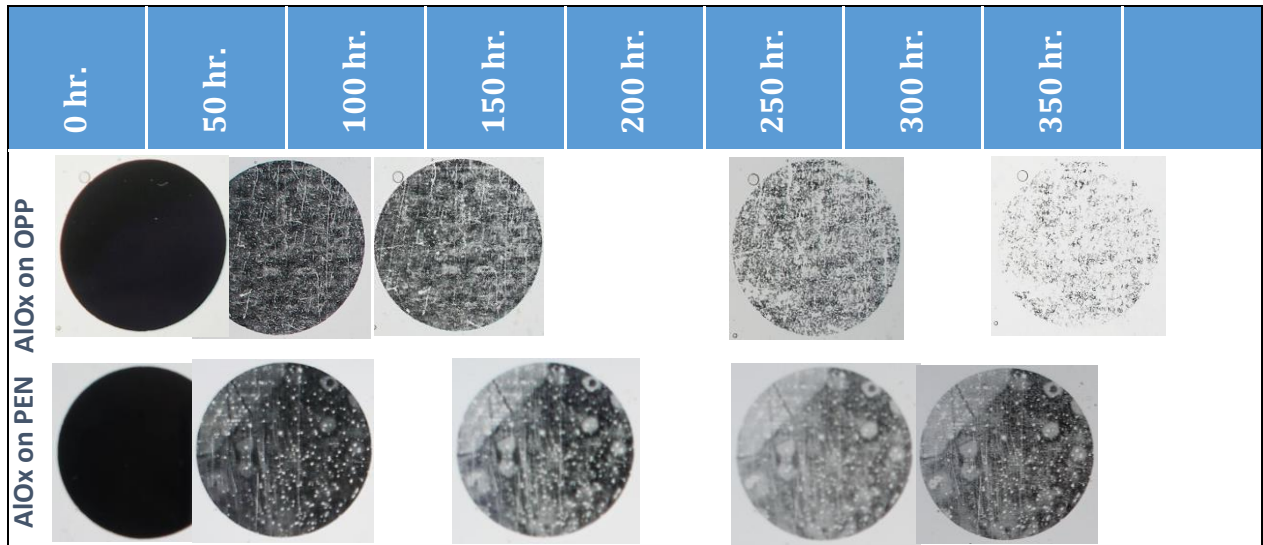


Figure 5 Optical images of Ca test samples from AlOx on OPP and on PEN taken at various times, as indicated at the top of the figure. The light grey area to the top left of the PEN images results from some sample (rather than material) defect, and should be ignored.

3.2 Deposition power

Having shown that transport of water vapour through our oxide layers is through a combination of macro- and nano- defects, we used the layers on OPP, which are more heavily controlled by the nano-defect permeation than those on PEN, to explore whether the nature or density of the defects can be modified by changes in the deposition conditions, in this case the sputtering power. The greater power applied to the sputter cathodes deposits more material for each time the sample passed the deposition source,

thus the number of passes was adjusted to lead to an approximately constant thickness of the coating for each sample. This is schematically illustrated in Fig 6(a).

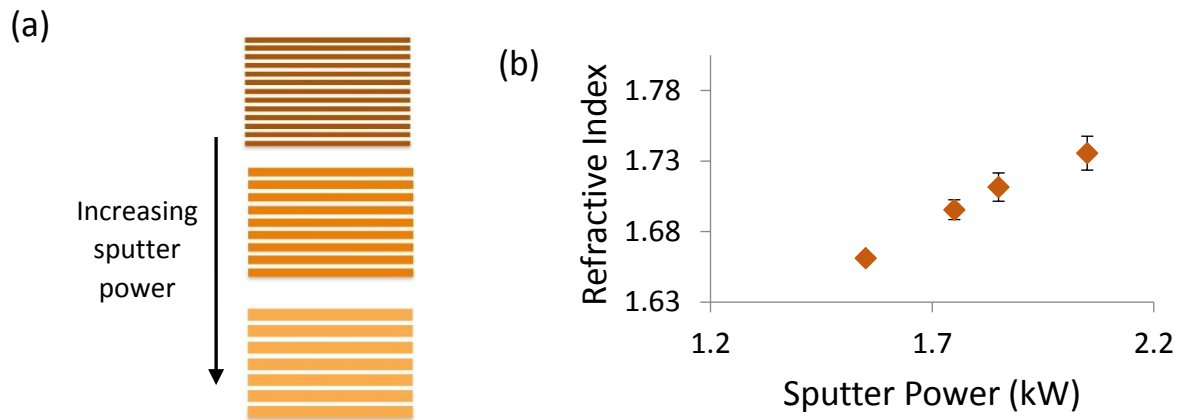


Figure 6 (a) Schematic illustrating the constant coating thickness at different sputter powers made up of a smaller number of sublayers each of greater thickness as the sputter power increases; (b) Refractive index of the AlOx coating (all of about 110nm in thickness) on OPP as a function of sputter power during AlOx deposition, as measured by ellipsometry.

The nature of the oxide is modified with sputter power (in the range 1.55 to 2.05kW), as illustrated with the refractive index increasing approximately linearly with power (Figure 6(b)), however the chemical composition (from XPS) of the coating does not appear to have significantly changed with power (Table 4). Erlat [18] related the increased 'density' of films, as evidenced by the increased refractive index, with improvements in barrier performance.

Table 4 Chemical compositions of the surface of oxide layers deposited onto OPP at different sputtering powers, as measured with XPS.

Power (kW)	Al (%)	O (%)	N (%)	C (%)	Ar (%)
1.55	37.7	56.5	1.0	4.8	<0.1
1.85	40.3	56.9	1.8	<0.1	1.0
2.05	39.0	55.7	1.3	4.0	<0.1

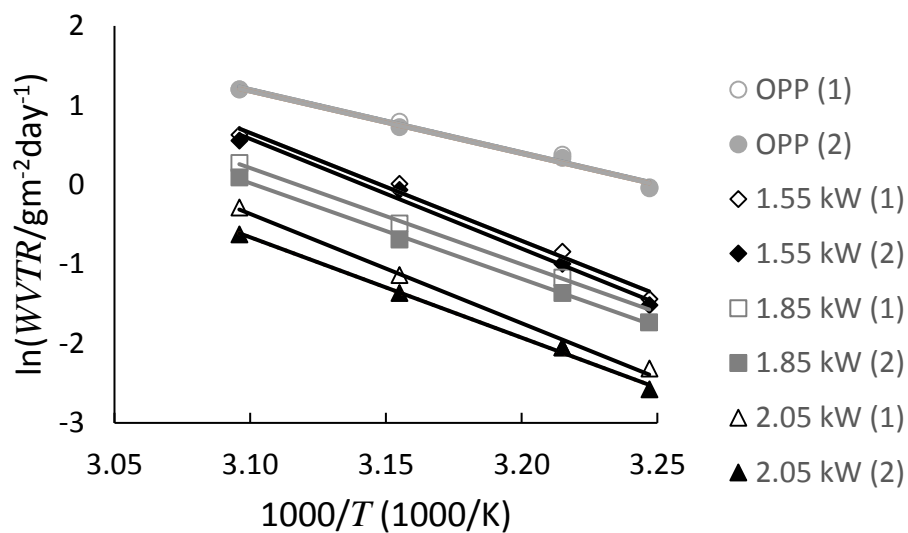


Figure 7 WVTR data for OPP/AIOx films with the oxide layer deposited at various powers, compared with data from the uncoated polymer. The activation energy is proportional to the gradient of the trends. The samples (1) and (2) at each power relate to two different samples tested in each of the sample chambers of the Permatran.

Table 5 Summary of water vapour permeation properties, comparing the different deposition powers. The permeability of the coating is calculated from the measured permeation of the composite using ideal laminate theory. The lowest value of permeation is taken for the permeability calculation and subsequent analysis, as this is least likely to be affected by any defects that may be induced by sample handling.

Film Power (kW)	Coating Thickness (nm)	WVTR at 38°C (g.m ⁻² .day ⁻¹)	ΔE_c (kJ.mol ⁻¹)	BIF	Permeability (μm.g.m ⁻² .day ⁻¹)
0 (polymer)	-	1.43	67	-	182.5
1.55	113	0.37, 0.43	113, 115	4, 3	0.056 (coating)
1.85	117	0.21, 0.23	100, 100	7, 6	0.037 (coating)
2.05	109	0.13, 0.13	105, 114	11	0.016 (coating)

The permeation data are summarised in Table 5. As seen in Figure 7 WVTR data for OPP/AlO_x films with the oxide layer deposited at various powers, compared with data from the uncoated polymer. The activation energy is proportional to the gradient of the trends. WVTR decreases as the sputter power increases, with all barriers showing permeation with activation energy in excess of 100kJ.mol⁻¹ indicating that a significant proportion of the permeation is through nano-defects. However the greatest activation energy (the 1.55kW sample) is once more associated with the greatest permeation, suggesting that in this instance greater permeation is associated with a greater proportion of the permeation being through nano-defects, or alternatively that the nature of the nano-defects is changing with sputter power such that the activation energy of permeation changes. **Error!**

Reference source not found. considers example data for the case in which the proportion of permeation through nano-defects changes, while the nature of the nano-defect permeation, parameterised by ΔE_{nd} , is constant. The case in which the WVTR is greatest, for the 1.55

kW sample, the activation energy is also greatest, and can be modelled with the proportion of permeation being through nano-defects ($WVTR_{nd}/WVTR_c$) being the greatest, at 64%. We observe that although there appears to be no simple trend in activation energy with power (the minimum activation energy being associated with the middle power level, 1.85kW experimentally, and in the sample data), there is a systematic decrease in each of the $WVTR_{md}$ and $WVTR_{nd}$ with each increase in power.

Table 6 Example data for a model of WVTR and ΔE_c , comparing the data for 110nm thick AlOx barriers on OPP deposited at different powers from Table 5. The value of ΔE_p is determined from WVTR measurements on the uncoated polymer. The value of ΔE_{nd} is arbitrarily set constant at 130 kJmol⁻¹ to simulate the case in which the interaction between the coating and the water during permeation through nano-defects is constant, and the different behaviour is because of a difference in the density of defects.

		1.55 kW	1.85 kW	2.05 kW
Macro-defects	WVF_{md} (g/m ² /day)	2.4 x 10 ¹⁰	2.2 x 10 ¹⁰	1.2 x 10 ¹⁰
	ΔE_p (kJ/mol) †	67	67	67
	$WVTR_{md}$ at 38°C (g/m ² /day)	0.14	0.13	0.05
Nano-defects	WVF_{nd} (g/m ² /day)	16.1 x 10 ²⁰	5.9 x 10 ²⁰	4.4 x 10 ²⁰
	ΔE_{nd} (kJ/mol)	130	130	130
	$WVTR_{nd}$ at 38°C (g/m ² /day)	0.24	0.09	0.06
Total	$WVTR_c$ at 38°C (g/m ² /day)	0.37	0.21	0.13
	ΔE_c (kJ/mol)	113	100	105
	$WVTR_{nd}/WVTR_c$	64%	41%	49%

An alternative model for the data could consider a constant value of WVF_{md} , but with varying ΔE_{nd} with power, in this case modelling the case in which the nature of the

permeant/defect interactions change with the changing nature of the defects as a result of sputtering conditions.

Table 7 Example data for a model of WVTR and ΔE_c , comparing the data for 110nm thick AlOx barriers on OPP deposited at different powers from Table 5. The value of ΔE_p is determined from permeation measurements on the uncoated polymer. The value of the value of WVF_{md} is arbitrarily set constant at 1.5×10^{10} , to simulate the case in which the density of macro-defects is constant, and the different behaviour is because of a difference in interaction between the water vapour and the coating.

		1.55 kW	1.85 kW	2.05 kW
Macrodefects	WVF_{md} (g/m ² /day)	1.5×10^{10}	1.5×10^{10}	1.5×10^{10}
	ΔE_p (kJ/mol) †	67	67	67
	$WVTR_{md}$ at 38°C (g/m ² /day)	0.08	0.08	0.08
Nanodefects	WVF_{nd} (g/m ² /day)	9.6×10^{19}	3.2×10^{18}	8.1×10^{22}
	ΔE_{nd} (kJ/mol)	121	115	144
	$WVTR_{nd}$ at 38°C (g/m ² /day)	0.29	0.13	0.05
Total	$WVTR_c$ at 38°C (g/m ² /day)	0.37	0.21	0.13
	ΔE_c (kJ/mol)	113	100	105
	$WVTR_{nd}/ WVTR_c$	77%	60%	36%

As can be seen from **Error! Reference source not found.**, the different powers give rise to differing nano-defect activation energy, although not in a steadily increasing fashion. For all values for WVF_{md} tried, a steady increase in ΔE_{nd} could not be found.

The Ca test morphologies (Figure 8) support the decreased flux of water vapour with increased sputter power measured by the MOCON, and that the morphology development

is the same in all cases with reasonably uniform greying in which no specific localised permeation resolved.

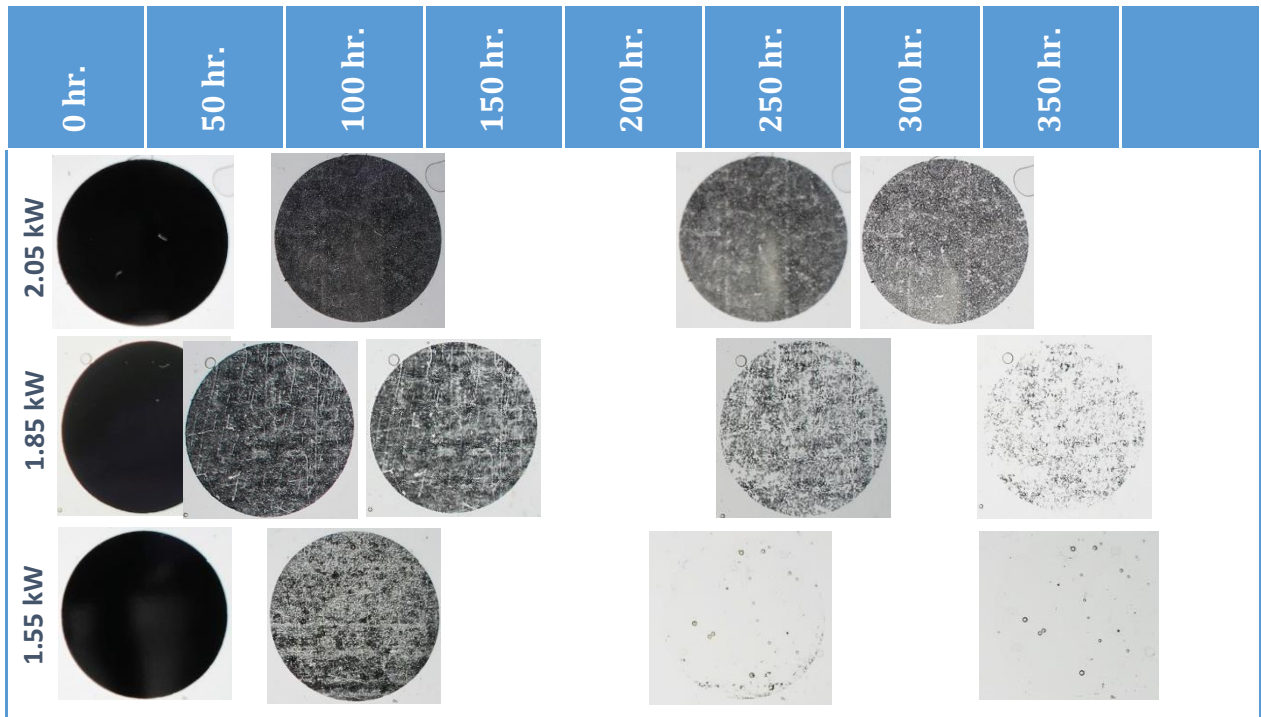


Figure 8 Optical images of Ca test samples taken at various times as indicated at the top of the figure, from AlOx on OPP deposited at various sputtering powers.

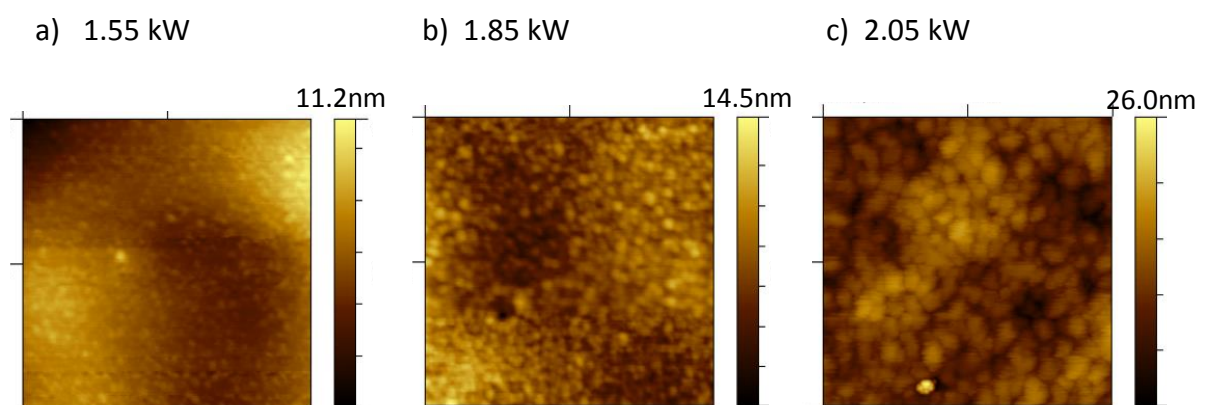


Figure 9 AFM images, 1 μm x 1 μm, of AlOx coatings, deposited at different sputtering power, on OPP substrates, showing the increase in agglomerate size with increasing power.

AFM characterisation of the oxides (Figure 9) revealed that the agglomerate size of the oxide increases with increased sputter power. This is potentially associated with the greater energy of the species arriving at the surface during deposition, with more mobility of the arriving species, allowing them to arrange themselves in larger agglomerates, as arriving species can move to find an existing nucleated AlO_x site on which to attach [31]. If the agglomerate boundaries are associated with defects, the density of these decreases with increased power, consistent with the trend in parameters in table 6. Note that if defects are associated with agglomerate boundaries, even in the case of the largest agglomerate size (greatest power) the density of these defects is such that they would not be individually resolved by the Ca test, consistent with the general 'greying' of the Ca with time.

In summary, with greater sputter power, larger agglomerates are formed, with a lower density of defects between them. This could be associated with the decreasing number of defects observed at higher power (table 6), and thus lower composite *WVTR*, but as the proportion of nano- to macro- permeation changes through the power series, so does the apparent activation energy.

3.3 Coating thickness

In a separate sequence of experiments, the thickness of the coating can be controlled simply by the number of sublayers deposited at a fixed sputter power (in this case 1.85 kW) as illustrated in Fig 10(a). Figure 10(b) shows how the refractive index of the coating material decreases with increased coating thickness.

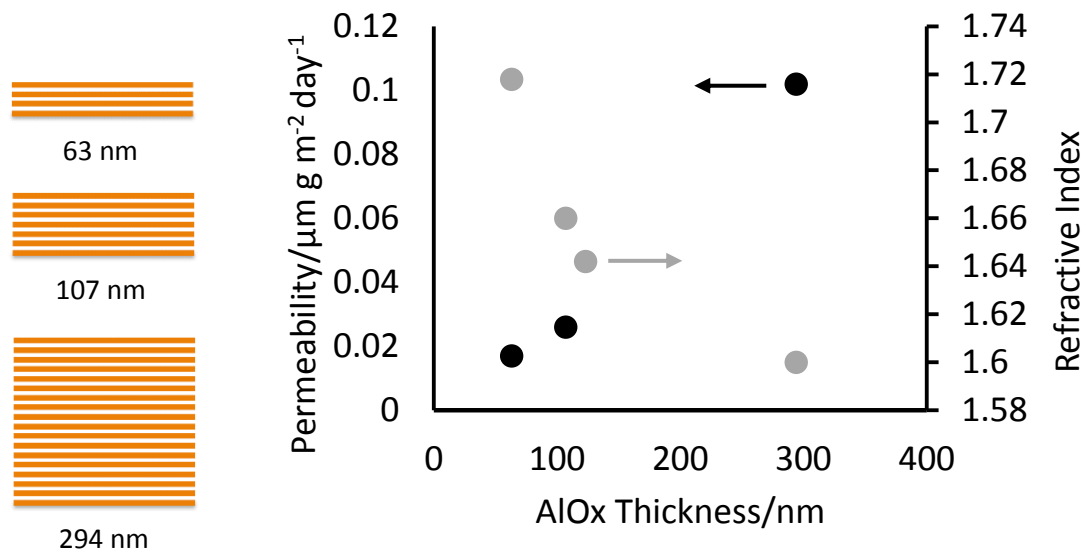


Figure 10 (a) Schematic illustrating the increasing coating thickness at constant sputter power made up of an increasing number of sublayers of constant thickness; (b) Permeability (black circles) and refractive index (grey circles) as a function of coating thickness.

Table 8 Summary of water vapour permeation properties, comparing the different coating thicknesses. The permeability of the coating is calculated from the measured permeation of the composite using ideal laminate theory. The lowest value of permeation is taken for the permeability calculation and subsequent analysis, as this is least likely to be affected by any defects that may have been induced by sample handling.

Oxide Film Thickness (nm)	WVTR at 38°C (g/m ² /day)	Activation Energy (kJ/mol)	Permeability ($\mu\text{m. g/m}^2/\text{day}$)
0 (substrate)	1.43	67	128.7 (substrate)
63	0.23	70	0.017
107	0.21, 0.23	76, 81	0.026
294	0.52, 0.37, 0.32, 0.28	85, 94, 96, 99	0.102

Table 8 summarizes the water vapour transport through barriers of different thickness. The Arrhenius plots from which these data are extracted are given in the appendix (Figure 11).

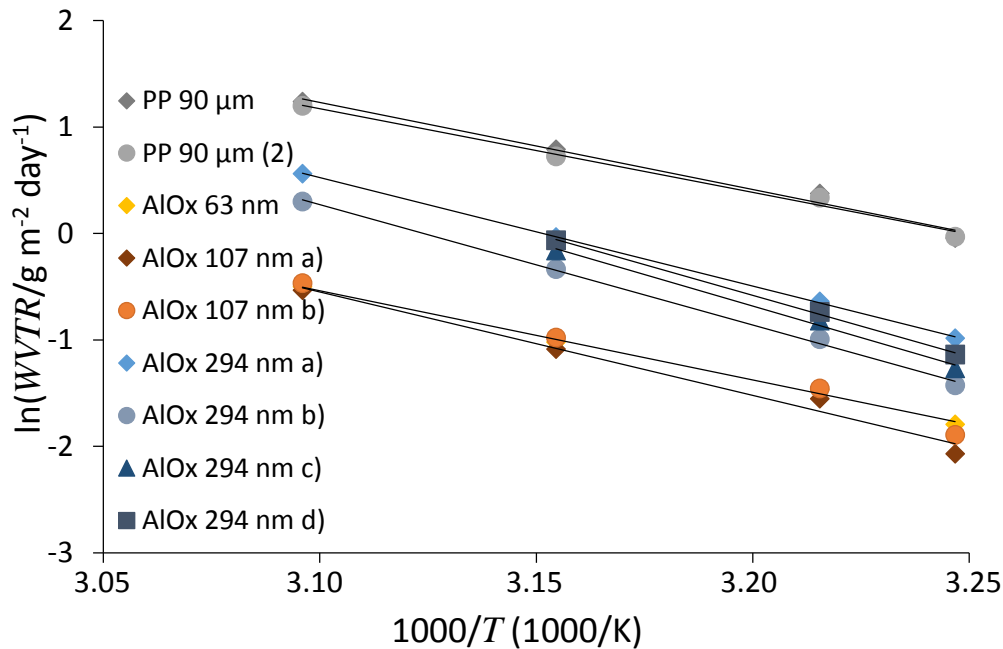


Figure 11 WVTR data for OPP/AlOx films with the oxide layer deposited at various powers, compared with data from the uncoated polymer. The activation energy is proportional to the gradient of the trends. The samples (1) and (2) at each power relate to two different samples tested in each of the sample chambers of the Permatran. Two sets of samples were tested of the thickest oxide.

As the barrier thickness increases, the permeability increases up to sixfold over the range tested. Thus, although there is no catastrophic loss of barrier due to the build-up of internal stresses, there is some reduction in barrier performance of the material, perhaps due to stresses induced in successive layers leading to a more open structure i.e. more nano-defects. This is commensurate (Figure 10b) with the observed decrease in refractive index

of the coating that might be associated with a lower density. Although as the barrier thickness increases the permeability increases, the activation energy also increases, suggesting that a greater proportion of the permeation takes place through nano-defects, in line with the hypothesis of a less dense film. Ca test data (Figure 12) show a similar morphology of Ca decay for all thicknesses, with a sufficiently high defect density in the coatings that individual defects are not resolved, as expected for this substrate polymer. This is a further example in which the activation energy rises as the films show a greater permeability, which can be described in terms of an increased proportion of the permeation taking place through nano-defects in the coating. Table 9 gives parameters consistent with this model.

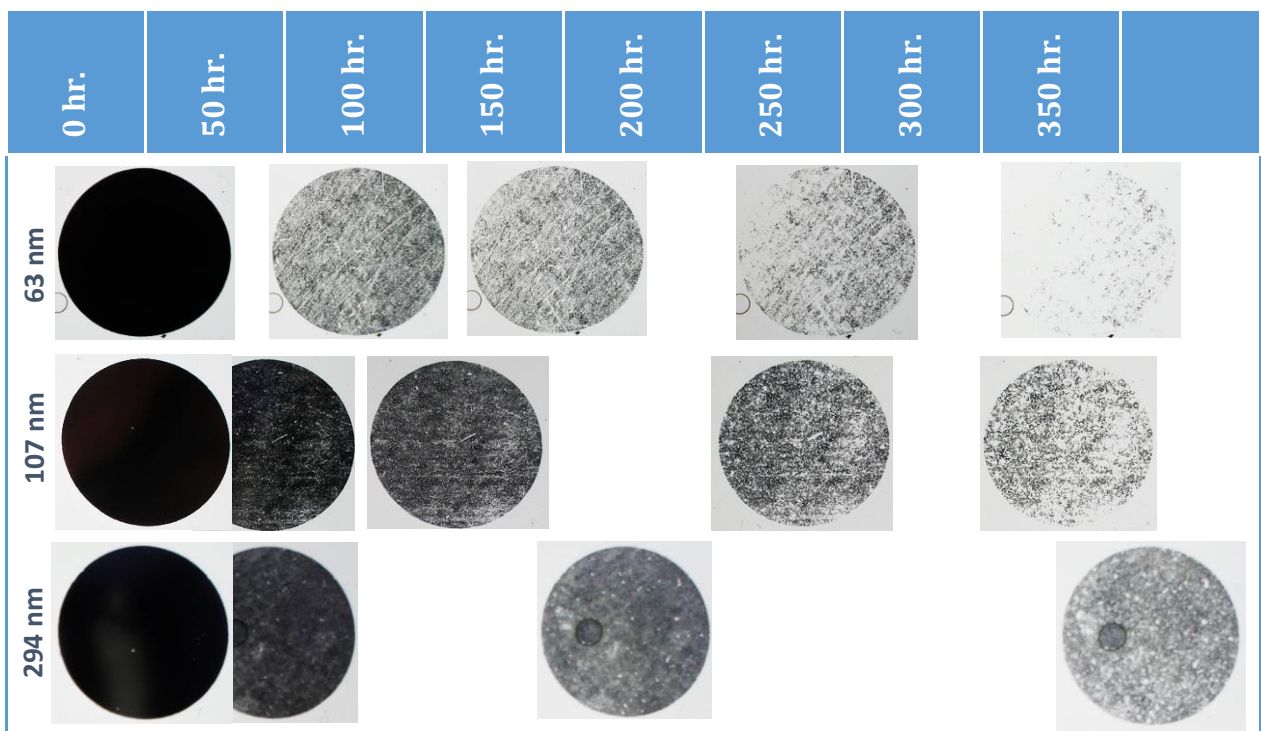


Figure 12 Calcium test comparing three films of increasing thickness AlOx.

Table 9 Example data for a model of WVTR and ΔE_c , comparing the data for AlOx barriers of different thickness deposited at 1.85 kW on OPP from Table 5. The value of ΔE_p is determined from permeation measurements on the uncoated polymer. The value of ΔE_{nd} is arbitrarily set constant at 130 kJmol^{-1} to simulate the case in which the interaction between the coating and the water during permeation through nanodefects is constant, and the different behaviour is because of a difference in the density of defects.

		63 nm	107 nm	294 nm
Macrodefects	$WV F_{md}$ (g/m ² /day)	4.0×10^{10}	3.4×10^{10}	3.0×10^{10}
	ΔE_p (kJ/mol) [†]	67	67	67
	$WVTR_{md}$ at 38°C (g/m ² /day)	0.22	0.19	0.17
Nanodefects	$WV F_{nd}$ (g/m ² /day)	0.5×10^{20}	1.4×10^{20}	7.6×10^{20}
	ΔE_{nd} (kJ/mol)	130	130	130
	$WVTR_{nd}$ at 38°C (g/m ² /day)	0.01	0.02	0.11
Total	$WVTR_c$ at 38°C (g/m ² /day)	0.23	0.21	0.28
	ΔE_c (kJ/mol)	70	76	99
	$WVTR_{nd}/WVTR_c$	3%	9%	40%

4. Conclusions

Thick AlOx barrier layers can be deposited on polymer substrates by sputter deposition of multiple thin sublayers without the increase in WVTR associated with really thick monolithic oxides. These thick layers allow sufficient coating of underlying defects that the barrier performance is not dominated by permeation through the macro-defects and thus the activation energy for permeation is seen to be greater than that of the underlying substrate. Where permeation is due to a combination of flux through macro-defects and nano-defects the relative proportion of permeation through these routes will control the apparent

activation energy observed. Thus, as the nano-defect nature and density can be affected by materials and processing parameters, it becomes important to measure the contribution to permeation due to these nano-defects.

Smooth substrates with only a small number of large defects in the oxide, such as those on PEN, show a high effective activation energy and low *WVTR*. In comparison, a polymer surface that gives rise to a rough oxide surface, even between the larger (taller) defects, can lead to a greater proportion of nanod defect-mediated permeation and hence a greater net *WVTR* while increasing further the effective activation energy.

Similarly, where the sputter power is increased, the grain size observed in the oxide is increased. If grain boundaries are associated with defects, then the density of these is decreased with increased sputtering power, explaining the lower *WVTR*. The changes in the proportion of permeation through nanod defects controls the effective activation energy observed with increasing sputter power. As the thickness of the oxide increases there is a decrease in refractive index which correlates to an increase in permeability of the AlO_x barrier material, which can be linked to an increase in the proportion of permeation occurring through nano-defects due to the associated increase in activation energy.

Thus, the effective activation energy can be a useful tool in understanding the nature of permeation, as well as being important to predict the behaviour of a particular barrier under different operating temperatures. Once the macro-defect density has been sufficiently reduced that there is a significant proportion of the permeant passing through nano-defects, then the effective activation energy is seen to increase. At this point it becomes important to consider means to reduce nano-defect permeation as well as macro-defect routes. Three examples demonstrated here relate to the nature of the polymer surface

between large asperities, the agglomerate size (in this case, controlled by sputter power) of the oxide and stress in the oxide.

Acknowledgements

This work was funded by EPSRC studentships with financial support, and provision of substrates, from DuPont Teijin Films and from Innovia Films. Data associated with this publication can be found at in the Oxford University data repository DOI:

10.5287/bodleian:kebvAa0y8

The authors are grateful for Dr Phil Holdway and Dr Hugh Bishop for XPS measurements, Dr Sverre Myhra for AFM measurements, and Dr David Scurr for ToF SIMS measurements.

References

- [1] A.G. Erlat, M. Yan, A.R. Duggal, Substrates and Thin-Film Barrier Technology for Flexible Electronics, in: A. Salleo & W.S. Wong (Eds.), *Flexible Electronics: Materials and Applications*, Springer, USA, 2009, pp 413-442.
- [2] J.-S. Park, H. Chae, H. K. Chung, S. I. Lee, Thin film encapsulation for flexible AM-OLED: a review, *Semiconductor Science and Technology* 26 (2011) 034001.
- [3] S.B. Jin, J.S. Lee, Y.S. Choi, J.G. Han, Gas Barrier properties of SiON films deposited by plasma enhanced chemical vapour deposition at low temperature as a function of the plasma process parameters, *Surface Coatings Technology* 228 (2013) S490-S494.
- [4] M. Top, S. Schönfeld, J. Fahlteich, S. Bunk, T. Kühnel, S. Straach, J. T. De Hosson, Hollow-cathode activated PECVD for the high-rate deposition of permeation barrier films, *Surface Coatings Technology* 314 (2017) 155-159.
- [5] J.A. Bertrand, S.M. George, Evaluating Al₂O₃ gas diffusion barriers grown directly on Ca films using atomic layer deposition techniques, *J. Vac Sci Technol. A Vacuum surfaces Film* 31 (2013) 01A122.
- [6] U. Soo Lee, J. Sik Choi, B. Seob Yang, S. Oh, Y. Jang Kim, M. Sook Oh, J. Heo, H. Joon Kim, Formation of a bilayer of ALD-SiO₂ and sputtered Al₂O₃/ZrO₂ films on Polyethylene Terephthalate Substrates as a moisture barrier, *ECS Solid State Lett* 2 (2013) R13-15.
- [7] D.-S. Han, D.-K. Choi, K.-W. Park, Al₂O₃/TiO₂ multilayer thin films grown by plasma enhanced atomic layer deposition for organic light-emitting diode passivation, *Thin Solid Films* 552 (2014) 155-158.

- [8] C.Y. Park, J.S. An, H.J. Jang, J.H. Lee, B.H. Choi, Growth behaviour and improved water-vapor-permeation-barrier properties of 10-nm-thick single Al₂O₃ layer grown via cyclic chemical vapour deposition on organic light-emitting diodes, *Org. Electron. Physics, Mater. Appl.* 15 (2014) 1717-1723.
- [9] P. Motamedi, K. Cadien XPS analysis of AlN thin films deposited by plasma enhanced atomic layer deposition, *Appl. Surf. Sci.* 315 (2014) 104-109.
- [10] Y.H. Yang, L. Boiling, M.A. Priolo, J.C. Grunlan, Super gas barrier and selectivity of graphene oxide-polymer multilayer thin films, *Adv. Mater.* 25 (2013) 503-508.
- [11] F.J. Norton, Helium diffusion through glass, *J. Am. Ceram. Soc* 36 (1953) 90-96.
- [12] W.G. Perkins, D.R. Begeal Diffusion and permeation of He, Ne, Ar, Kr and D₂ through silicon oxide thin films, *J. Chem. Phys.* 54 (1971) 1683-1694.
- [13] V. Stannett in: J. Crank (Ed) Diffusion in polymers, Academic Press, London 1968 (Chapter 2).
- [14] A.P. Roberts, B.M. Henry, A.P.Sutton, C.R.M. Grovenor, G.A.D.Briggs, T. Miyamoto, M. Kano, Y. Tsukahara, M. Yanaka, Gas permeation in silicon-oxide/polymer (SiO_x/PET) barrier films: role of the oxide lattice, nano-defects and macro defects, *J. Membr. Sci* 208 (2002) 75-88.
- [15] A.S. da Silva Sobrinho, Transparent barrier coating on polyethylene terephthalate by single- and dual- frequency plasma-enhanced chemical vapour deposition, *J. Vac, Sci, Technol. A Vacuum, Surfaces, Film.* 18 (1998) 3190-3198.

- [16] A.G. Erlat, R.J. Spontak, R.P. Clarke, T.C. Robinson, P.D. Haaland, Y. Tropsha, N.G. Harvey, E. a. Vogler, SiO_x gas barrier coatings on polymer substrates: morphology and gas transport considerations, *J. Phys Chem B* 103 (1999) 6047-6055.
- [17] A.G Erlat, B.M. Henry, J.J. Ingram, D. B. Mountain, A. McGuigan, R.P. Howson, C.R.M.Grovenor, G.A.D.Briggs, Y. Tsukahara, Characterisation of aluminium oxynitride gas barrier films, *Thin Solid Films* 388 (2001) 78-86.
- [18] A.G. Erlat, B. Henry, C. Grovenor, A. Briggs, R. Chater, Y. Tsukahara, Mechanism of water vapor transport through PET/AlO_xN_y Gas barrier Films, *J. Phys Chem B* 108 (2004) 883-890.
- [19] B. Henry, A.G. Erlat, A. McGuigan, C.R. Grovenor, G.A.Briggs, Y. Tsukahara, T. Miyamoto, N. Noguchi, T. Niijima, Characterization of transparent aluminium oxide and indium tin oxide layers on polymer substrates, *Thin Solid Films* 382 (2001) 194-201.
- [20] B. Henry, F. Dinelli, K.-Y. Zhao, C.R. Grovenor, O. Kolosov, G.A. Briggs, A. Roberts, R. Kumar, R. Howson, A microstructural study of transparent metal oxide gas barrier films' *Thin Solid Films* 355-356 (1999) 500-505.
- [21] H. Chatham, Review Oxygen diffusion barrier properties of the transparent oxide coating on polymeric substrates, *Surf. Coating Technol.* 78 (1996) 1-9.
- [22] G. Rossi, M. Nulman, Effect of local flaws in polymeric permeation reducing barriers, *J. Appl. Phys.* 74 (1993) 5471-5475.
- [23] A. Grüniger, Ph. Rudolf von Rohr, Influence of defects in SiO_x thin films on their barrier properties, *Thin Solid Films* 459 (2004) 308-312.

- [24] M. Hanika, H.C. Langowski, U. Moosheimer, W. Peukert, Inorganic Layers on Polymeric Films – Influence of defects and morphology on barrier properties, *Chem. Eng. Technol.* 26 (2003) 605-614.
- [25] E. Toni, M.G. Baschetti, C. Lorenzetti, P. Fayet, G.C. Sarti, Effects of random defect distributions in the barrier coating on the gas permeability of multilayer films, *Surface and Coatings Technology* 302 (2016) 65-74.
- [26] B.M. Henry, A.G.Erlat, C.R.M. Grovenor, C-S Deng, G.A.D. Briggs, T. Miyamoto, N. Noguchi, T. Nijima, Y. Tsukahara, The permeation of water vapor through gas barrier films, *44th Annual Technical Conference Proceedings, Society of Vacuum Coaters* 44 (2001) 469-475.
- [27] J.T. Felts, Thickness effects on thin film gas barrier: silicon-based coatings, *Soc. Vac. Coaters 34th Annu. Tech. Conf, Proc.* 34 (1991) 99-104.
- [28] Y. Leterrier, J. Andersons, Y. Pitton, J.E. Manson, Adhesion of silicon oxide layers on poly(ethylene terephthalate). II: effect of coating thickness on adhesive and cohesive strengths, *J. Polym. Sci Part B* 35 (1997) 1463-1472.
- [29] B.M. Henry, A.J. Topping, A. Searle, H.E. Assender, C.R.M. Grovenor, M. Creatore, M.C.M. van de Sanden, Barrier properties of transparent multilayer films, *50th Annual Technical Conference Proceedings, Society of Vacuum Coaters* 50 (2007) 217-220.
- [30] Y.H. Choi, Y.G. Lee, X. Bulliard, K.H. Lee, S. Lee, D. Choi, J.J. Park, J.M. Kim, Homogeneous Al₂O₃ multilayer structures with reinforced mechanical stability for high-performance and high-throughput thin-film encapsulation, *Scripta Materialia* 62 (2010) 447-450.

[31] K. Wasa, S. Hayakawa, Handbook of sputter deposition technology: principles, technology and Applications, Noyes, USA, 1992.